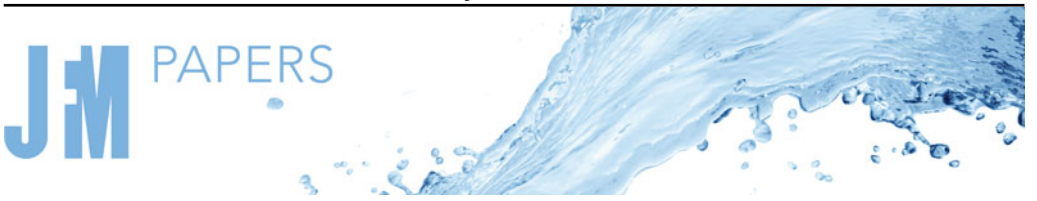
J. Fluid Mech. (2026), *vol.* 1043, A11, doi:10.1017/jfm.2026.12036



Viscoplastic interactions tune collective dynamics of microswimmers

Yan Xia[1], **Zhaosheng Yu**[2], **Zhaowu Lin**[2] **and Takuji Ishikawa**[1]

[1]Department of Biomedical Engineering, Tohoku University, Sendai 980-8579, Japan

[2]State Key Laboratory of Fluid Power and Mechatronic System, Department of Mechanics, Zhejiang University, Hangzhou 310027, PR China

Corresponding authors: Takuji Ishikawa, t.ishikawa@tohoku.ac.jp; Zhaowu Lin, linzhaowu@zju.edu.cn

(Received 1 March 2026 UTC; revised 16 July 2026 UTC; accepted 13 August 2026 UTC)

Viscoplastic fluids flow only when stress exceeds the yield stress, confining swimmer-induced flows within the yield surface and limiting far-field hydrodynamic interactions. We investigate how yield stress tunes collective dynamics of microswimmers in monolayer suspensions. Higher yield stress shifts the phase transition in puller suspensions to higher densities and weakens flocking of spherical neutral swimmers, governed by the ratio of yield stress to swimmer density. In ellipsoidal swimmers, collisions dominate, making yield stress less influential. These systems constitute a distinct category in which hydrodynamic interactions are cut off, providing new insight into the long-standing debate about the impact of far- and near-field hydrodynamics on collective dynamics of microswimmers.

Key words: collective behaviour, active matter, plastic materials

1. Introduction

Active-matter systems, such as self-propelled colloids and microorganisms, exhibit a wide range of collective behaviours, stemming from their inherently out-of-equilibrium nature (Ramaswamy 2010; Elgeti *et al.* 2015; Gompper 2025). In a liquid medium, self-propelled particles interact via hydrodynamic forces and steric effects. These interactions lead to rich collective dynamics, such as mobility-induced phase separation (MIPS) that produces aggregates (Fily & Marchetti 2012; Cates & Tailleur 2015), flocks with polar alignment (Ishikawa *et al.* 2008; Bricard *et al.* 2013) and chaotic vortex patterns known as bacterial turbulence (Dombrowski *et al.* 2004; Aranson 2022).

© The Author(s), 2026. Published by Cambridge University Press. This is an Open Access article, distributed under the terms of the Creative Commons Attribution licence (https://creativecommons.org/licenses/by/4.0/), which permits unrestricted re-use, distribution and reproduction, provided the original article is properly cited.

https://doi.org/10.1017/jfm.2026.12036 Published online by Cambridge University Press

The impact of hydrodynamic interactions (HIs) on collective behaviour has been emphasised by comparing active Brownian particles that consider only the excluded-volume (steric) effect (Bechinger *et al.* 2016; Zöttl & Stark 2023) with squirmers that account for full hydrodynamics (Lighthill 1952; Blake 1971). A squirmer is a self-propelled particle with a surface slip velocity; it is called a 'puller' when the anterior thrust is stronger, and a 'pusher' when the posterior thrust is stronger (Ishikawa 2024). Mobility-induced phase separation has been widely reported in active Brownian particles, whereas studies of squirmers suggest that it is less likely to occur when HIs are fully taken into account (Theers *et al.* 2018; Zhou & Brady 2026). In contrast, MIPS-like clustering can emerge for strong puller squirmers (Ishikawa 2008; Kyoya *et al.* 2015). This phenomenon suggests that the underlying mechanism differs from standard MIPS driven solely by motility and steric effects; rather, the clustering is mediated by HIs between strong puller squirmers. The effects of HIs require further clarification.

In Stokes flow, where inertia is negligible, the flow field induced by a microswimmer propagates over long distances, giving rise to HIs (Lauga & Powers 2009; Lauga 2020). Throughout this paper, we distinguish the flow field outside the lubrication region (referred to as the outer region) from that within the lubrication region (the inner region), with a crossover at a surface-to-surface distance of approximately $0.5-1$ particle radii (Brady & Bossis 1988; Kim & Karrila 2005). This terminology is adopted to avoid confusion with the conventional use of the term far field in the active-matter literature, where it usually refers to the asymptotic force-dipole flow. The flow field in the outer region corresponds to the outer solution of lubrication theory and can be calculated with significantly greater accuracy than point-stresslet approximations. For spherical particles, this approach yields highly accurate predictions of particle motion down to surface-to-surface separations of the order of $0.5-1$ particle radii. Due to the outer-region HIs, non-spherical swimmers align in the extensional direction, inducing collective swimming (Aditi Simha & Ramaswamy 2002; Saintillan & Shelley 2008). When swimmers come into close proximity, HIs in the inner region, mediated by lubrication flows, become significant (Ishikawa *et al.* 2006), together with steric effects (Kantsler *et al.* 2013). Considerable debate has therefore persisted regarding whether HIs originating from the outer region or the inner region, or steric effects, are primarily responsible for the observed collective behaviour (Kim & Karrila 2005; Ishikawa *et al.* 2008; Saintillan & Shelley 2008; Drescher *et al.* 2011; Wensink 2012; Redner *et al.* 2013; Kyoya *et al.* 2015; Bechinger *et al.* 2016; Yoshinaga & Liverpool 2018; Qi *et al.* 2022; Zöttl & Stark 2023; Wu-Zhang *et al.* 2024; Ishikawa 2025; Zhou & Brady 2026). In the Stokes flow regime, however, both contributions are intrinsically coupled and always present simultaneously, making it difficult to isolate their respective roles and draw definitive conclusions.

To date, numerous insights have been accumulated regarding swimming in non-Newtonian fluids (Wu *et al.* 2020; Spagnolie & Underhill 2023). Collective dynamics in non-plastic, non-Newtonian fluids has also been widely reported (Li & Ardekani 2016; Tung *et al.* 2017; Aceves-Sanchez *et al.* 2020; Liu *et al.* 2021; Liao & Aranson 2023; Kobayashi *et al.* 2024; Zhang *et al.* 2024; Zhang *et al.* 2025; Chamolly & Ishikawa 2026). In viscoelastic fluids, for instance, fluid elasticity modulates the local HIs between swimmers and promotes collective swimming (Li & Ardekani 2016; Tung *et al.* 2017; Liao & Aranson 2023).

In contrast to non-plastic non-Newtonian fluids, viscoplastic fluids can restrict their spatial extent due to the presence of a yield stress; examples include mud, slurry, mucus and blood. Consequently, far-field HIs can be effectively eliminated in viscoplastic fluids, whereas they are unavoidable in Stokes flows of Newtonian fluids. This is because a microswimmer induces flow only within the yielded region, and the unyielded regions

https://doi.org/10.1017/jfm.2026.12036 Published online by Cambridge University Press

behave as solid rather than fluid (Balmforth & Hewitt 2025). This property of viscoplastic fluids is ideal for eliminating only far-field HIs, offering a distinct setting that differs from previous studies. We note that, in a viscoplastic fluid, the stress field does not necessarily vanish outside the yielded region. However, the cutoff of far-field HIs can be understood in a dynamical sense, since HIs between swimmers are conventionally defined as flow-mediated couplings, whereby the velocity disturbance generated by one squirmer induces the translational and rotational motion of another. While the behaviour of a single swimmer (Hewitt & Balmforth 2017; Eastham *et al.* 2022; Hewitt & Balmforth 2022; Nazari *et al.* 2023; Xia *et al.* 2025*c*) and two-swimmer interactions (Xia *et al.* 2025*a*) in viscoplastic fluids have been examined, collective behaviour in viscoplastic fluids remains unexplored.

In this paper, using full hydrodynamic simulations, we investigate the collective dynamics of a monolayer of squirmers embedded in a viscoplastic medium. Strong pullers form MIPS-like clusters via HIs, but increasing the yield stress and inhibiting far-field HIs hinder their formation. Spherical neutral squirmers exhibit flocking with polar alignment, but increasing the yield stress suppresses its formation. The flocking is governed by the range of HIs and can be collapsed using yield stress and areal fraction of swimmers, underscoring the role of far-field HIs. In contrast, flocking in ellipsoidal neutral squirmers is only weakly affected by yield stress, indicating the dominance of near-field HIs and steric effects. This indicates a qualitatively different mechanism of collective behaviour between spherical and ellipsoidal swimmers. These findings are uniquely enabled by the use of a viscoplastic fluid, providing new insight into the long-standing debate on the relative importance of far- and near-field HIs on collective dynamics.

2. Model description

2.1. *Basic equations*

To model swimmers, we employ the squirmer model in spherical or ellipsoidal form (figure 1). The parameters b_x and b_z denote the semi-minor and semi-major axes, defining the aspect ratio $a_r = b_z/b_x$ and effective radius $a = \sqrt{b_x b_z}$. The modified prolate spheroidal coordinate system that we use is given by (ζ, τ, φ) (the details are explained in Appendix A). The surface slip velocity of an ellipsoidal squirmer is given by (Ishikawa *et al.* 2006; Theers *et al.* 2018)

$$\boldsymbol{u}_s = -B_1(1+\beta\zeta)\big(\boldsymbol{e}_\zeta \cdot \boldsymbol{p}\big)\boldsymbol{e}_\zeta, \tag{2.1}$$

where $\boldsymbol{p}$ is the unit orientation vector of the squirmer and $\boldsymbol{e}_\zeta$ is the unit polar vector. The constant B_1 determines the swimming velocity of a solitary squirmer $v_0 = B_1\tau_0$ $(\tau_0 - (\tau_0^2 - 1)\coth^{-1}\tau_0)$ in the Stokes limit, with $\tau_0 = (1 - a_r^{-2})^{-1/2}$ (Keller & Wu 1977; Theers *et al.* 2016). For $b_z = b_x = a$, the surface velocity for a spherical squirmer is recovered to $\boldsymbol{u}_s = B_1 \sin\theta(1+\beta\cos\theta)\boldsymbol{e}_\theta$, where θ represents the polar angle, while $\boldsymbol{e}_\theta$ is the unit tangent vector along the θ direction (see figure 1*b*). The active stress β helps in categorising the types of squirmer as pusher ($\beta < 0$), puller ($\beta > 0$) and neutral swimmer ($\beta = 0$). Here we focus specifically on the cases $\beta = 0$ and $\beta = \pm 3$.

The full HIs between swimmers in a viscoplastic fluid are resolved by solving the Navier–Stokes equations using a fictitious domain method (Xia *et al.* 2025*c*), while the steric interactions between swimmers are captured using a repulsive force model (Ishikawa *et al.* 2006) to avoid the prohibitively small time step needed to overcome the overlapping particles. The basic concept of the fictitious domain method is to fill the interior of the particles with a 'fictitious' fluid and to locally apply a forcing term $\boldsymbol{f}$ that enforces the boundary conditions on the particle surfaces and accounts for fluid–solid

https://doi.org/10.1017/jfm.2026.12036 Published online by Cambridge University Press

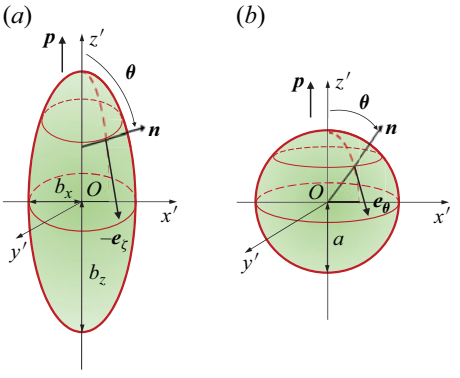


Figure 1. Model for (*a*) an ellipsoidal squirmer and (*b*) a spherical squirmer.

interactions. The flow field is simulated by solving the Navier–Stokes equations in the whole domain including the volume occupied by the particles:

$$\rho_f \left(\frac{\partial \boldsymbol{u}}{\partial t} + \boldsymbol{u} \cdot \boldsymbol{\nabla} \boldsymbol{u} \right) = \boldsymbol{\nabla} \cdot (-p\boldsymbol{I} + \boldsymbol{\tau}) + \boldsymbol{f}, \tag{2.2}$$

$$\boldsymbol{\nabla} \cdot \boldsymbol{u} = \boldsymbol{0}. \tag{2.3}$$

Here, $\boldsymbol{u}$, p and ρ_f represent the fluid velocity, pressure and density, respectively. We employ a simple Bingham model, for which the shear-stress tensor reads

$$\begin{aligned} \boldsymbol{\tau} &= \left(2\mu + \frac{\tau_y}{\dot{\gamma}} \right) \dot{\boldsymbol{\gamma}} \quad \text{for} \quad \tau > \tau_y, \\ \dot{\boldsymbol{\gamma}} &= \boldsymbol{0} \quad \text{for} \quad \tau \leqslant \tau_y, \end{aligned} \tag{2.4}$$

where $\boldsymbol{\tau}$ denotes the stress tensor, τ_y is the yield stress, μ is the viscosity constant and $\dot{\boldsymbol{\gamma}} = \boldsymbol{\nabla} \boldsymbol{u} + \boldsymbol{\nabla} \boldsymbol{u}^T$ is the strain-rate tensor. Here $\tau \equiv \sqrt{(1/2)\boldsymbol{\tau} : \boldsymbol{\tau}}$ and $\dot{\gamma} \equiv \sqrt{(1/2)\dot{\boldsymbol{\gamma}} : \dot{\boldsymbol{\gamma}}}$ refer to the second invariants of the stress and strain-rate tensors, respectively. Swimmer velocity $\boldsymbol{U}$ and angular velocity $\boldsymbol{\omega}$ obey Newton's equations of motion:

$$\rho_s V_p \frac{\mathrm{d}\boldsymbol{U}}{\mathrm{d}t} = \int_S \boldsymbol{n} \cdot (-p\boldsymbol{I} + \boldsymbol{\tau}) \, \mathrm{d}s, \tag{2.5}$$

$$\frac{\mathrm{d}\,(\boldsymbol{J} \cdot \boldsymbol{\omega})}{\mathrm{d}t} = \int_S \boldsymbol{r} \times \left[\boldsymbol{n} \cdot (-p\boldsymbol{I} + \boldsymbol{\tau}) \right] \mathrm{d}s. \tag{2.6}$$

Here, V_p and $\boldsymbol{J}$ are the swimmer volume and moment of inertia tensor, respectively, ρ_s is the density of swimmers and $\boldsymbol{r}$ is the position vector with respect to the particle centre of mass.

The position $\boldsymbol{X}$ of each swimmer is determined from the following kinematic equation:

$$\frac{\mathrm{d}\boldsymbol{X}}{\mathrm{d}t} = \boldsymbol{U}. \tag{2.7}$$

The orientation of swimmers is determined by

$$\frac{\mathrm{d}\boldsymbol{q}}{\mathrm{d}t} = \frac{1}{2} \begin{pmatrix} q_4 & -q_3 & q_2 & q_1 \\ q_3 & q_4 & -q_1 & q_2 \\ -q_2 & q_1 & q_4 & q_3 \\ -q_1 & -q_2 & -q_3 & q_4 \end{pmatrix} \begin{pmatrix} \omega_x' \\ \omega_y' \\ \omega_z' \\ 0 \end{pmatrix}. \tag{2.8}$$

https://doi.org/10.1017/jfm.2026.12036 Published online by Cambridge University Press

In (2.8), q_1, q_2, q_3 and q_4 are the components of the unit quaternion, which can be defined in terms of the Euler angles (Yu & Shao 2007). The components of the angular velocity, ω_x', ω_y' and ω_z', are measured in the body-fixed frame. With the quaternion, the rotation matrix from the space-fixed frame to the body-fixed frame reads

$$\boldsymbol{R} = 2\begin{pmatrix} q_1^2+q_4^2-\frac{1}{2} & q_1q_2+q_3q_4 & q_1q_3-q_2q_4 \\ q_1q_2-q_3q_4 & q_2^2+q_4^2-\frac{1}{2} & q_2q_3+q_1q_4 \\ q_1q_3+q_2q_4 & q_2q_3-q_1q_4 & q_3^2+q_4^2-\frac{1}{2} \end{pmatrix}. \tag{2.9}$$

Since the swimmer is rotationally symmetric, its orientation $\boldsymbol{p}$ is fully determined by the direction of its symmetry axis, the z' axis, in the space-fixed frame. The orientation vector is given by $\boldsymbol{p} = \boldsymbol{R} \cdot (0, 0, 1)^T$.

The fictitious domain method for modelling the swimming of a spherical or ellipsoidal squirmer in a Newtonian fluid has been validated in our previous studies (Lin & Gao 2019; Xia *et al.* 2025*d*). The accuracy of the method in simulating particle sedimentation (Yu & Wachs 2007) and swimming dynamics of a squirmer (Xia *et al.* 2025*c*) in viscoplastic fluids has also been verified. Further details of the numerical implementation can be found in Appendix A.

2.2. *Simulation set-up*

The suspension consists of N swimmers in a computational box with size $[L, L, H]$. The centres and orientations of all swimmers are restricted to the mid-plane of the box, i.e. a monolayer. We use periodic boundary conditions in the x and y directions while the boundary conditions for velocity and pressure on the top and bottom boundaries are $\partial \boldsymbol{u}/\partial z = \boldsymbol{0}$ and $\partial p/\partial z = 0$, respectively. The influence of the boundaries in the z direction is negligible, since the fluid behaves as a solid outside the yielded region (figure 2). The areal fraction of swimmers is given by $\phi_a = N\pi a^2/L^2$. The dynamics of our system is governed by the Bingham number,

$$Bi = \frac{\tau_y a}{\mu B_1}, \tag{2.10}$$

which measures the ratio between the yield stress and viscous stress.

In our previous research (Kyoya *et al.* 2015), we investigated a monolayer of spherical or ellipsoidal squirmers in a Newtonian fluid, varying the aspect ratio from 1 to 3. The results show that the behaviour at an aspect ratio of 3 differed markedly from that at spherical shape, whereas the difference at an aspect ratio of 2 was less pronounced, indicating that the influence of aspect ratio becomes significant at higher values. Based on these findings, we focus on an aspect ratio of 3 for ellipsoidal swimmers in the present study.

The simulation box of size $L = 32a$ and $H = 16a$ is discretised in a three-dimensional uniform grid with mesh number $N_x \times N_y \times N_z = 512 \times 512 \times 256$. For the calculations presented in this work, 32 grid points are used across the particle's diameter ($2a/\Delta x = 32$) and the time step is set to be $0.001a/B_1$; each is run for a duration exceeding $1000a/B_1$, and various parameters are monitored to ensure reaching statistically steady states. The numerical convergence of the method for swimming in viscoplastic fluids has been validated in our previous study (Xia *et al.* 2025*a*,*c*) through systematic grid refinement. The swimmers were initially placed with random orientations. We choose a small but finite Reynolds number $Re = \rho_f B_1 a/\mu = 0.1$. The effect of the domain width L (as well as the

https://doi.org/10.1017/jfm.2026.12036 Published online by Cambridge University Press

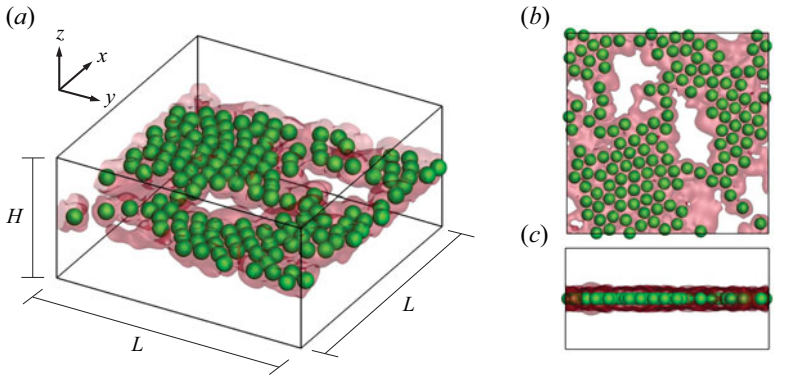


Figure 2. Schematic representation of the model system. The red iso-surface represents the yield surface defined by $\tau = \tau_y$ for the representative parameters $Bi = 0.1$ and $\beta = 0$. (*a*) Three-dimensional perspective view, (*b*) cross-section in the $x-y$ plane and (*c*) cross-section in the $y-z$ plane.

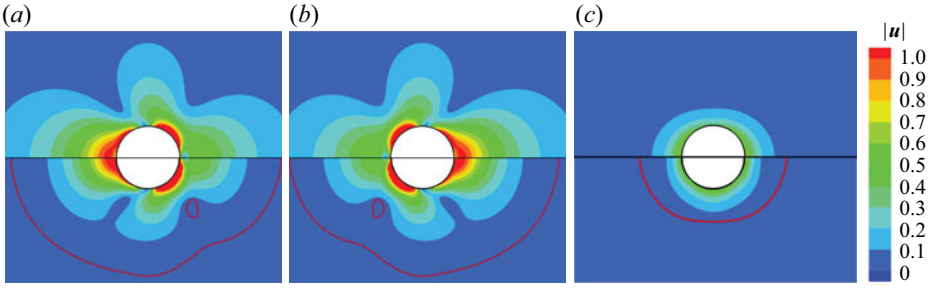


Figure 3. Magnitude of the disturbance velocity induced by a single squirmer for (*a*) $\beta = 3$, (*b*) $\beta = -3$ and (*c*) $\beta = 0$. In each panel, the upper half shows the Newtonian case ($Bi = 0$), while the lower half shows the viscoplastic cases ($Bi = 0.1$). The red contours delineate the yield surface in the viscoplastic fluid.

swimmer number N) has been examined by using a larger width $L = 64a$ in Appendix B, which indicates that the domain size does not influence the conclusions from our work.

2.3. *Flow disturbance by a solitary squirmer*

To establish a baseline of viscoplasticy-mediated HIs, we first examine the flow fields around a solitary puller, pusher or neutral swimmer in both Newtonian and viscoplastic environments. Since a detailed report has already been presented in Xia *et al.* (2025*c*), we provide only a brief overview here. Figures 3 and 4 compare the disturbance flow fields in the Newtonian fluid with those at $Bi = 0.1$ and 1, respectively. As expected, the flow field at $Bi = 0.1$ closely resembles the Newtonian solution, whereas increasing the Bingham number progressively confines the disturbance to a finite yielded region. At $Bi = 1$, viscoplasticity effectively screens the long-range disturbance generated by the squirmers. The magnitude of the flow inside the yielded region is also altered relative to the Newtonian case. These observations indicate that viscoplasticity does not simply 'remove' outer-region HIs. Rather, it accelerates the spatial decay of the disturbance flow.

https://doi.org/10.1017/jfm.2026.12036 Published online by Cambridge University Press

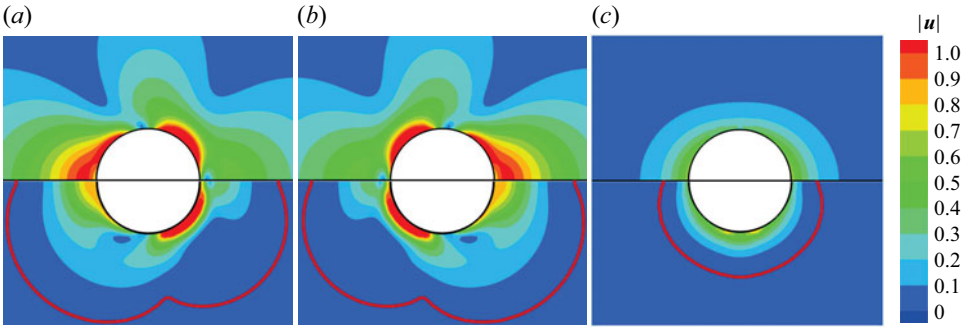


Figure 4. Magnitude of the disturbance velocity induced by a single squirmer for (*a*) $\beta = 3$, (*b*) $\beta = -3$, and (*c*) $\beta = 0$. In each panel, the upper half shows the Newtonian case ($Bi = 0$), while the lower half shows the viscoplastic cases ($Bi = 1$). The red contours delineate the yield surface in the viscoplastic fluid.

At a small Bingham number, the size of the yielded region can be estimated by balancing the stress induced by the squirmer with the yield stress. For a puller or pusher, we have

$$\tau(r) \sim \frac{S}{r^3} \sim \tau_y, \tag{2.11}$$

where $S \sim \mu v_0 a^2$ is the stresslet. This balance gives a characteristic yielded radius R_Y as

$$R_Y \sim \left(\frac{S}{\tau_y}\right)^{1/3}. \tag{2.12}$$

Then we have

$$\frac{R_Y}{a} \sim Bi^{-1/3}. \tag{2.13}$$

For a neutral swimmer, whose leading-order disturbance is a source dipole decaying as $u \sim v_0(a/r)^3$ and the associated stress scales as $\tau(r) \sim \mu v_0 a^3/r^4$. Balancing this stress with the yield stress gives

$$\frac{R_Y}{a} \sim Bi^{-1/4}. \tag{2.14}$$

In a homogeneous monolayer suspension, the average separation between swimmers scales as $d/a = (\pi\phi_a)^{-1/2}$. Then we expect that the yielded radius compared with the average particle separation scales as $R_Y/d \sim Bi^{-1/3}\phi_a^{1/2}$ (pushers/pullers) or $Bi^{-1/4}\phi_a^{1/2}$ (neutral swimmers).

3. Results

3.1. *Clustering of pullers*

We begin by considering suspensions of puller squirmers ($\beta = 3$). In Newtonian suspensions, strong pullers tend to aggregate into clusters (Ishikawa 2008; Kyoya *et al.* 2015). However, in a viscoplastic fluid, the yield stress can dissolve the aggregation (figure 5). To visualise the degree of packing inside clusters, we employ the bond parameter $\psi_{6,k} \in [0, 1]$ that measures local sixfold bond orientational order of swimmer k (Zöttl & Stark 2014), where $\psi_{6,k} \equiv (1/6)|\sum_{j\in N_6^k} \exp(i6\vartheta_{kj})|$. Here the sum goes over the six nearest neighbours of swimmer k, and ϑ_{kj} is the angle between the reference direction and the line connecting the particle k and its neighbouring particle j. We

https://doi.org/10.1017/jfm.2026.12036 Published online by Cambridge University Press

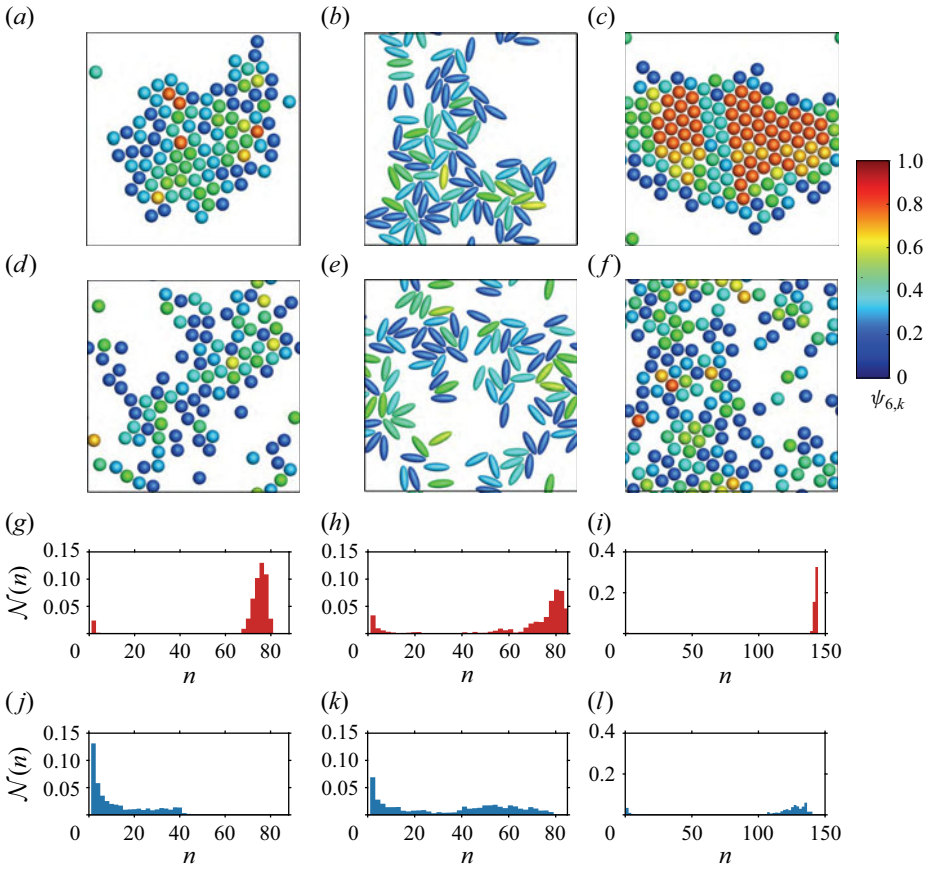


Figure 5. The MIPS-like clustering in puller suspensions ($\beta = 3$). Snapshots of the system showing collective behaviour in (*a–c*) a Newtonian fluid and (*d–f*) a viscoplastic fluid with $Bi = 1$: (*a*,*d*) $\phi_a = 0.25$, $a_r = 1$, (*b*,*e*) $\phi_a = 0.25$, $a_r = 3$ and (*c*,*f*) $\phi_a = 0.45$, $a_r = 1$. All individual squirmers are coloured by the local bond-orientational order $\psi_{6,k}$, ranging between 0 (dislocations and disclinations) and 1 (hexagonal crystal). (*g–l*) Cluster-size distribution functions $\mathcal{N}(n)$ in (*g–i*) a Newtonian fluid and (*j–l*) a viscoplastic fluid.

show the colour-coded bond parameter in figure 5(*a–f*). Specifically, the cluster of both spherical and ellipsoidal pullers with $\phi_a = 0.25$ is progressively destroyed by yield stress, where no long-lived clusters exist (see also supplementary movies available at https://doi.org/10.1017/jfm.2026.12036). In a denser suspension ($\phi_a = 0.45$), the cluster exhibits pronounced hexagonal ordering (figure 5*c*). As the Bingham number Bi increases, the resulting structure becomes progressively weaker and less coherent.

To quantify our findings, we identify the cluster structure using the cluster-size distribution function (Levis & Berthier 2014; Be'er *et al.* 2020; Qi *et al.* 2022). Clusters are identified using a distance criterion: a particle is assigned to a cluster if its nearest neighbour within that cluster satisfies $\epsilon \leqslant a/4$, where ϵ is the surface-to-surface distance. The normalised cluster-size distribution function is defined as

$$\mathcal{N}(n) = \frac{\langle np(n) \rangle}{N}. \tag{3.1}$$

Here $\langle \cdot \rangle$ denotes temporal averaging in the steady regime. The normalised cluster-size distribution function gives the fraction of particles belonging to clusters of size n, where

https://doi.org/10.1017/jfm.2026.12036 Published online by Cambridge University Press

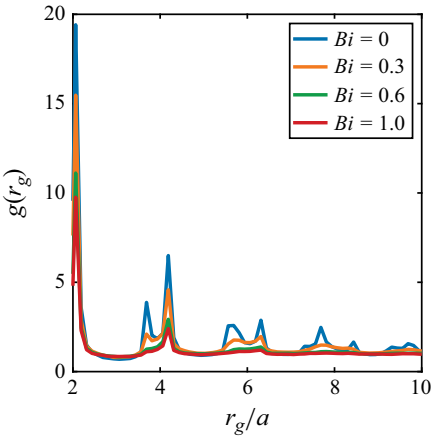


Figure 6. Pair-correlation function of spherical pullers ($\beta = 3$) at $\phi_a = 0.3$ with increasing Bi.

$p(n)$ is the number of clusters containing n particles. In a Newtonian fluid, we observe a bimodal cluster-size distribution with a pronounced peak at large n, indicating phase separation. At $Bi = 1$, the second peak of $\mathcal{N}(n)$ diminishes and vanishes at $\phi_a = 0, 25$ (figure 5*g*,*h*), demonstrating the strong suppression of phase separation by yield stress on puller clustering. For denser cases ($\phi_a = 0.45$; figure 5*i*,*l*), the second peak weakens with increasing yield stress, but remains visible even at $Bi = 1$.

In order to quantify puller aggregation, the pair-correlation function is introduced as

$$g(r_g) = \frac{\left\langle \sum_{i\neq j}^{N} \delta\left(r_g - r_{ij}\right)\right\rangle}{2\pi n r_g}, \tag{3.2}$$

where r_{ij} is the centre–centre distance of swimmer pairs and $n = N/L^2$ is the average number density of swimmers in the plane.

The aggregation $g(r_g)$ of spherical pullers with increasing Bingham number at $\phi_a = 0.3$ is shown in figure 6. In all cases, the first peak of $g(r_g)$ locates at around $r_g \simeq 2a$, representing the strong tendency of attraction between squirmer pairs. The peak value of $g(r_g)$ decreases with Bi, suggesting a weakening of effective attraction due to yield stress.

We introduce the expectation of $\mathcal{N}(n)$, i.e.

$$E_{\mathcal{N}} = \frac{\sum_{n=1}^{N} n\mathcal{N}(n)}{N}. \tag{3.3}$$

Physically, $E_{\mathcal{N}} \in [0, 1]$ provides a measure of the degree of clustering: higher values indicate that particles are more concentrated in larger clusters, while lower values suggest that particles are more uniformly distributed. Here we focus on spherical pullers. Figure 7(*a*) shows $E_{\mathcal{N}}$ plotted versus ϕ_a for several values of Bi. The curves exhibit an increasing sigmoidal shape, where the steep region corresponds to the transition from the gas-like to the cluster state. In a Newtonian fluid, this transition is relatively sharp, whereas it becomes progressively smoother as Bi increases.

According to figures 7(*a*) and 5(*g–i*), we define the cluster state corresponding to $E_{\mathcal{N}} \geqslant 0.5$ while $\mathcal{N}(n)$ has a second peak. Figure 7(*b*) determines a diagram in the

https://doi.org/10.1017/jfm.2026.12036 Published online by Cambridge University Press

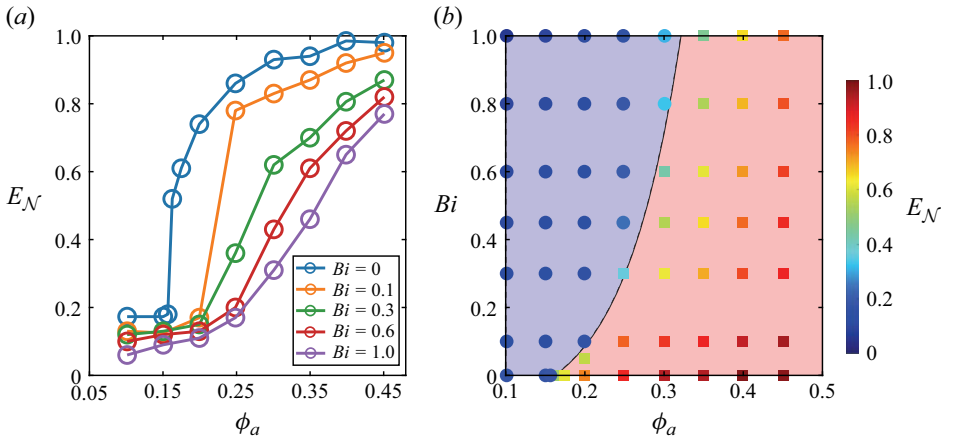


Figure 7. Cluster formation of pullers ($\beta = 3$). (*a*) The value $E_\mathcal{N}$ as a function of the areal fraction at different Bi. (*b*) State diagram in the parameter space of ϕ_a versus Bi. We identify the cluster state (squares) when a second peak appears in the cluster-size distribution function, whereas the gas-like state (circles) corresponds to a single-peak distribution. The pink and blue background regions indicate the clustered and gas-like phases, respectively.

parameter space of ϕ_a versus Bi for pullers. In general, the pullers exhibit a cluster state in the regime with higher values of ϕ_a and lower values of Bi.

We demonstrate that MIPS-like clustering weakens with increasing yield stress as outer-region HIs are cut off, indicating that outer-region HIs play a key role in cluster formation. Correspondingly, the onset of clustering is shifted to higher area fraction (i.e. smaller average particle separation) and becomes more gradual as Bi increases. This behaviour can be interpreted as a competition between hydrodynamic attraction, which promotes aggregation, and decorrelating effects such as rotational diffusion. When viscoplasticity screens the disturbance flows, stronger crowding is required for hydrodynamic attraction to become dominant. The characteristic cluster size is also likely linked to the extent of the yielded region, since a smaller yielded zone reduces the effective range over which swimmers can interact and thereby suppresses the growth of large aggregates.

We note that the observed changes in collective behaviour should not be interpreted as arising solely from the direct removal of outer-region contributions. Rather, they likely result from a combined effect: the attenuation of long-range disturbances together with modifications of the flow field within the finite yielded region, which alter the local velocity and velocity-gradient fields experienced by nearby swimmers. The comparison with pusher suspensions presented in the following section, where no hydrodynamically mediated phase separation is observed, further highlights the crucial role of strong puller-induced HIs in driving the MIPS-like clustering reported here.

3.2. *Whirl structures of pushers*

We next examine the role of yield stress in the collective motion of pushers ($\beta = -3$). Previous studies in Newtonian fluids have established that elongated pushers tend to develop strong mesoscale spatiotemporal motions. We analyse the velocity correlation among pushers at $\phi_a = 0.3$ in figure 8. Here we use the surface-to-surface distance ϵ to emphasise the positive correlation among nearby swimmers. The correlation is calculated only when a swimmer is present lateral to the reference squirmer, i.e. $\pi/4 - 3\pi/4$ from its

https://doi.org/10.1017/jfm.2026.12036 Published online by Cambridge University Press

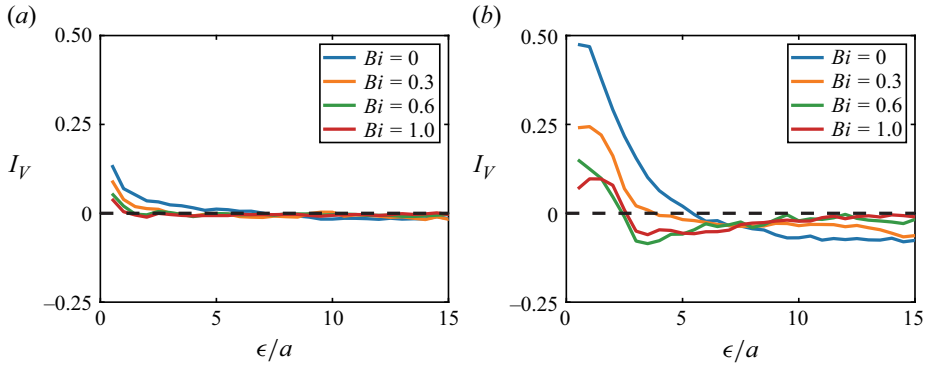


Figure 8. Effects of Bi on the whirl structures of pushers ($\beta = -3$) under $\phi_a = 0.3$. Spatial correlation of the particle velocity for (a) spherical and (b) ellipsoidal ($a_r = 3$) pushers.

orientation:

$$I_V(\epsilon) = \frac{\left\langle \sum_{i \neq j} \boldsymbol{U}(\boldsymbol{X}_i) \cdot \boldsymbol{U}(\boldsymbol{X}_j)\, \delta\big(\epsilon - \epsilon_{ij}\big) \right\rangle_{\frac{\pi}{4} \leqslant \theta_{ij} \leqslant \frac{3\pi}{4}}}{\left\langle \sum_{i \neq j} \delta\big(\epsilon - \epsilon_{ij}\big) \right\rangle_{\frac{\pi}{4} \leqslant \theta_{ij} \leqslant \frac{3\pi}{4}}}, \tag{3.4}$$

where $\theta_{ij} = \cos^{-1}(\boldsymbol{p}_i \cdot (\boldsymbol{X}_j - \boldsymbol{X}_i)/|\boldsymbol{X}_j - \boldsymbol{X}_i|)$ represents the angle between the squirmer orientation and the relative position vector of the squirmer pair.

The profile of I_V is positive in the small-ϵ region but negative in the large ϵ region, which defines the whirl structure. Notably, these correlations are significantly more robust in ellipsoidal pushers than in their spherical counterparts. This highlights the importance of steric effects in whirl structures, considering that HIs are comparable for ellipsoidal and spherical squirmers with the same β. As Bi increases, the magnitudes of the positive correlations decrease for small ϵ, indicating that HIs contribute to the formation of whirl structures. However, the persistence of whirl structures even at $Bi = 1.0$ highlights the importance of steric effects for ellipsoidal swimmers (see also supplementary movies). In elongated pusher suspensions, the extensile stresslet generates flow fields that attract nearby swimmers in the lateral direction. Hydrodynamic attraction brings swimmers into close proximity, where steric interactions arising from their elongated shape reorient them, leading to enhanced alignment and positive velocity correlations. Increasing plasticity is expected to weaken this alignment, as the range of the attractive flow is reduced.

3.3. *Flocking of neutral swimmers*

Finally, we consider suspensions of neutral squirmers ($\beta = 0$), which are known to exhibit flocks with polar alignment in Newtonian suspensions (Ishikawa *et al.* 2008; Bricard *et al.* 2013). The strength of ordering can be described by the global polar order parameter

$$P(t) = \frac{\left|\sum_i^N \boldsymbol{p}_i\right|}{N}. \tag{3.5}$$

Quantitatively, P exhibits distinct variation curves depending on Bi (figure 9*a*,*b*; $\phi_a = 0.3$). For spherical swimmers, when $Bi \leqslant 0.6$, the system evolves towards a steady

https://doi.org/10.1017/jfm.2026.12036 Published online by Cambridge University Press

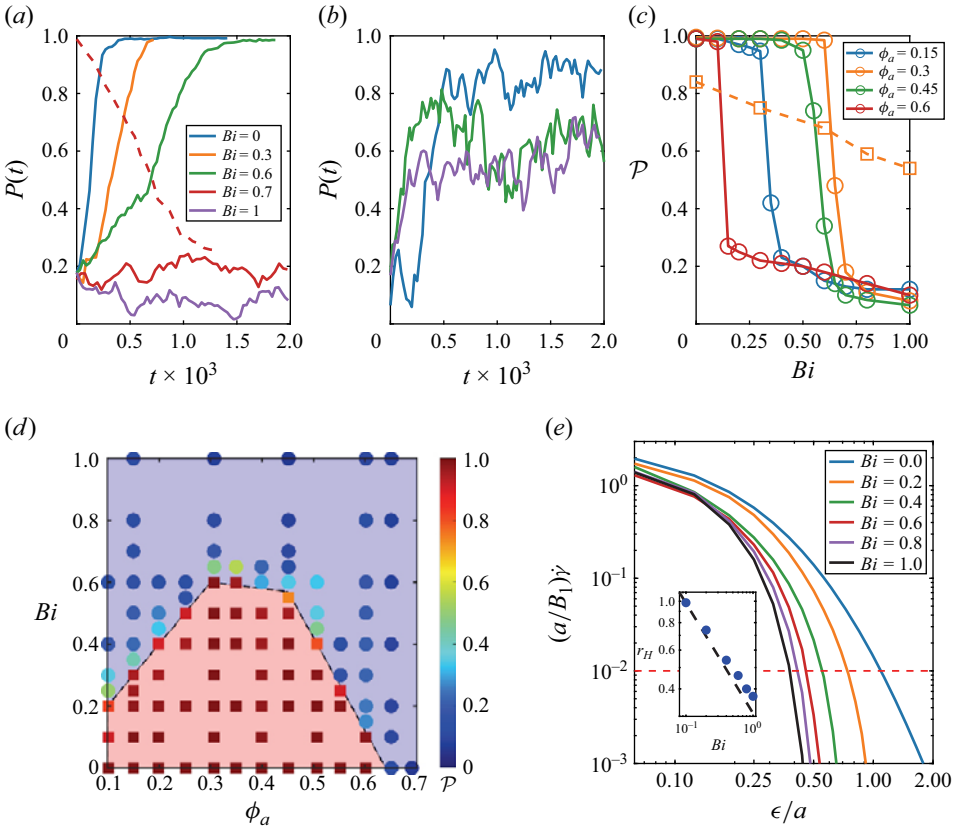


Figure 9. Effect of Bi on the polar order of neutral swimmers ($\beta = 0$). Temporal evolutions of the global polar order parameter at different Bi for (*a*) spherical and (*b*) ellipsoidal ($a_r = 3$) squirmers ($\phi_a = 0.3$). (*c*) Mean polarisation as a function of Bi with various ϕ_a; solid lines with circles correspond to spherical squirmers, while the dashed line with squares corresponds to ellipsoidal squirmers. (*d*) State diagram for spherical squirmers in the parameter space ϕ_a versus Bi. We define the polar-ordered phase corresponding to $\mathcal{P} \geqslant 0.7$. The blue and pink background regions indicate the disordered and ordered phases, respectively. (*e*) The second invariant of strain-rate tensor versus the distance ϵ relative to the surface of an isolated swimmer along the swimming direction. Inset: evaluated hydrodynamic range r_H as the distance at which the normalised strain rate becomes less than 10^{-2}; the dashed line corresponds to $r_H = 0.3Bi^{-1/2}$.

polar-ordered state ($P \to 1$). This ordering is purely hydrodynamic, as spheres possess no steric reorientation mechanism. Once Bi exceeds a critical threshold ($Bi_c \approx 0.65$), the system undergoes a transition from global order to global disorder ($P \ll 1$) (figure 9*a*). Even for initially aligned configurations at $Bi = 0.7$, the global polar order decays from perfect alignment, demonstrating that the ordered state is unstable at sufficiently large Bi. These results suggest that HIs play a crucial role in the emergence of polar order. These observations are also qualitatively consistent with our previous study of pairwise neutral squirmer interactions in viscoplastic fluids (Xia *et al.* 2025*a*). In a Newtonian fluid, HIs between two neutral squirmers promote reorientation towards a more aligned configuration following close interaction, whereas increasing the Bingham number weakens this alignment-promoting reorientation. The reduced tendency for pairwise alignment provides a plausible microscopic mechanism for the weaker orientational ordering observed in the present collective simulations.

https://doi.org/10.1017/jfm.2026.12036 Published online by Cambridge University Press

In contrast, ellipsoidal swimmers ($a_r = 3$) exhibit pronounced fluctuations in $P(t)$ (figure 9*b*) consistent with previous observations (Kyoya *et al.* 2015). This difference from spherical swimmers is mainly attributed to steric effects, suggesting that the observed fluctuations originate from steric interactions. Although they do not develop as strong an ordered state as spherical swimmers in a Newtonian medium, their ordering is markedly less sensitive to Bi. This reduced sensitivity stems from the steric effect to align with neighbouring ones, which dominates over HIs (Baskaran & Marchetti 2008). We further examine the combined effects of Bi and ϕ_a on the long-time mean polarisation $\mathcal{P} = \langle P(t) \rangle$. Figure 9(*c*) shows $\mathcal{P}$ as a function of Bi for $\phi_a = 0.15$ to 0.6. For spherical swimmers, $\mathcal{P}$ drops sharply when Bi exceeds a critical value, signalling a clear transition from ordered to disordered states. In contrast, for ellipsoidal swimmers, $\mathcal{P}$ decreases gradually with Bi, without exhibiting a well-defined transition, indicating a qualitative difference from spherical swimmers.

Our analysis produces a phase diagram (figure 9*d*) in the (ϕ_a, Bi) space that delineates the transition between ordered and disordered states for spherical swimmers. The red region indicates the presence of ordering among the swimmers, whereas in the blue region this ordering nearly vanishes. This polar order vanishes at high areal fraction. For ϕ_a smaller than 0.65, a well-defined critical Bingham number Bi_c can be identified for each ϕ_a. Interestingly, Bi_c exhibits a non-monotonic dependence on ϕ_a. The value of Bi_c reaches its maximum at $\phi_a \approx 0.3$. In the semi-dilute regime ($\phi_a \leqslant 0.3$), Bi_c increases approximately linearly with ϕ_a, whereas at higher areal fractions ($\phi_a \geqslant 0.45$), Bi_c drops sharply as ϕ_a increases.

We now rationalise the observed non-monotonic dependence of Bi_c on ϕ_a. Our results indicate that outer-region HIs are key in the development of polar order. In the semi-dilute regime, we assume that polar alignment is governed by HIs acting within an effective HI range r_H, over which HI-induced reorientation, governed by the local strain-rate tensor, remains significant. As shown in figure 9(*e*), $\dot{\gamma}$ decays rapidly along the swimming axis, and its magnitude is strongly suppressed with increasing Bi, indicating a reduction of r_H. Defining r_H as the distance at which the normalised strain rate becomes negligible ($(a/B_1)\dot{\gamma} < 10^{-2}$), we extract $r_H(Bi)$ and find an empirical scaling $r_H \propto Bi^{-1/2}$ (inset of figure 9*e*). Polar order can develop only when the typical nearest-neighbour distance $r_{nn} \sim \phi_a^{-1/2}$ is smaller than r_H. Equating $r_H = r_{nn}$ leads to the scaling $Bi_c \sim \phi_a$, consistent with the simulation results in figure 9(*d*), with $Bi_c \simeq 2\phi_a$ for $\phi_a \leqslant 0.3$. In contrast, as ϕ_a approaches the jamming areal fraction, the fluid throughout the middle plane is fully yielded, and the available free space between swimmers is strongly reduced, resulting in enhanced near-field HIs via lubrication forces. Because lubrication forces disrupt polar alignment (Ishikawa 2019), flocks become destabilised, leading to a decrease of Bi_c at high ϕ_a.

4. Conclusion

We investigated the collective dynamics of microswimmers embedded in a viscoplastic medium. This system constitutes a distinct class in which HIs can be effectively cut off, shedding new light on the long-standing debate regarding the respective roles of far- and near-field HIs in collective behaviour. Specifically, our results highlight the importance of outer-region HIs for spherical squirmers in forming MIPS-like clusters, whirls and flocking. In contrast, steric interactions play a crucial role for ellipsoidal squirmers.

The mechanisms discussed in the present work should also be distinguished from the long-wavelength hydrodynamic instability of infinitely extended suspensions of straight swimmers described by continuum kinetic theories (Saintillan & Shelley

https://doi.org/10.1017/jfm.2026.12036 Published online by Cambridge University Press

2007, 2008). Here, we focus on a confined microswimmer monolayer and investigate how viscoplasticity modifies the effective HI range governing the observed collective dynamics. The findings of this study provide general insight into the use of viscoplastic fluids as a means to tune collective behaviour in active suspensions.

In the absence of a yield stress, a strongly shear-thinning fluid (i.e. pseudo-plastic fluid) may also lead to a significant reduction of long-range HIs, and some of the observed features could potentially arise from this effect. A systematic comparison with shear-thinning fluids would be an interesting direction for future work.

Another important direction for future study is to extend the present monolayer configuration to fully three-dimensional suspensions. The HIs in a quasi-two-dimensional monolayer can differ fundamentally from those in an unconfined three-dimensional bulk system, where out-of-plane motion and three-dimensional structures may substantially modify collective motions. Investigating how viscoplasticity alters these genuinely three-dimensional hydrodynamic couplings would help clarify the universality of the mechanisms identified here and their relevance to active suspensions.

Supplementary movies. Supplementary movies are available at https://doi.org/10.1017/jfm.2026.12036.

Funding. The work was supported by the National Natural Science Foundation of China (grant nos. 12302340, 12132015 and 12332015), the JSPS KAKENHI (grant nos. 24KF0097, 21H04999 and 21H05308) and the JST CREST (grant no. JPMJCR25Q1).

Declaration of interests. The authors report no conflict of interest.

Appendix A. Numerical implementation

A.1. *The squirmer model*

The swimmer considered has a prolate spheroidal shape. In a body-fixed Cartesian coordinate, the equation describing the swimmer's surface reads

$$\frac{x^2+y^2}{b_x^2}+\frac{z^2}{b_z^2}=1, \tag{A1}$$

where b_x and b_z are the semi-minor and semi-major axes, respectively. We denote half of the focal length by $c=\sqrt{b_z^2-b_x^2}$, which yields the eccentricity $e=c/b_z$ ($0\leqslant e<1$, with $e=0$ describing a sphere). The prolate spheroidal coordinates (ζ,τ,φ) are related to the Cartesian coordinates (x,y,z) via

$$\zeta=\frac{1}{2c}\left(\sqrt{x^2+y^2+(z+c)^2}-\sqrt{x^2+y^2+(z-c)^2}\right), \tag{A2}$$

$$\tau=\frac{1}{2c}\left(\sqrt{x^2+y^2+(z+c)^2}+\sqrt{x^2+y^2+(z-c)^2}\right), \tag{A3}$$

$$\varphi=\arctan\left(\frac{y}{x}\right). \tag{A4}$$

In the equations, $-1\leqslant\zeta\leqslant 1$, $1\leqslant\tau$ and $0\leqslant\varphi<2\pi$. The body-fixed Cartesian coordinates of a point on the swimmer surface $\boldsymbol{r}_s=(x_s,y_s,z_s)^T$ are $x_s=b_x\sqrt{1-\zeta^2}\cos\varphi$, $y_s=b_x\sqrt{1-\zeta^2}\sin\varphi$ and $z_s=b_z\zeta$. All points with $\tau=\tau_0\equiv e^{-1}$ lie on the ellipsoid's surface. The unit vectors $\boldsymbol{e}_\tau$ and $\boldsymbol{e}_\zeta$ on the ellipsoid surface are related to those of the Cartesian

https://doi.org/10.1017/jfm.2026.12036 Published online by Cambridge University Press

coordinates via

$$\begin{aligned} \boldsymbol{e}_\tau &= \left(\frac{2\tau \cdot \sqrt{1-\zeta^2}}{\sqrt{\tau^2-1}} \boldsymbol{e}_x + \zeta \boldsymbol{e}_z \right) \cdot \frac{\sqrt{\tau^2-1}}{\sqrt{\tau^2-\zeta^2}}, \\ \boldsymbol{e}_\zeta &= \left(\frac{2\zeta \cdot \sqrt{\tau^2-1}}{\sqrt{1-\zeta^2}} \boldsymbol{e}_x + \tau \boldsymbol{e}_z \right) \cdot \frac{\sqrt{1-\zeta^2}}{\sqrt{\tau^2-\zeta^2}}. \end{aligned} \tag{A5}$$

In the squirmer model, the propulsion is generated by imposing surface squirming velocities. The surface velocity is assumed to be tangential, steady and axisymmetric. The general form of the surface velocity is expressed as (Blake 1971)

$$\boldsymbol{u}_s = -\sum_{n=1}^{\infty} \frac{2B_n}{n(n+1)} P_n'(\boldsymbol{p}\cdot\boldsymbol{n})\boldsymbol{p}\cdot(\boldsymbol{I}-\boldsymbol{n}\boldsymbol{n}), \tag{A6}$$

where $\boldsymbol{p}$ is the unit orientation vector, $\boldsymbol{n} = \boldsymbol{e}_\tau$ is the unit normal vector and $\boldsymbol{I}$ is the unit tensor. Here P_n' is the derivative of the nth-order Legendre polynomial. The coefficients B_n are often called polar modes. We consider the prescribed surface velocity (A6) with the first two polar modes (B_1 and B_2); then it is simplified as (2.1).

A.2. *Implementation of the fictitious domain method*

We employ the augmented Lagrangian method proposed by Dean & Glowinski (2002) for the solution of the constitutive equations (2.4), which are rewritten as

$$\boldsymbol{\tau} = 2\mu\dot{\boldsymbol{\gamma}} + \tau_y \boldsymbol{B}. \tag{A7}$$

Tensor $\boldsymbol{B}$ is a non-dimensional tensor which satisfies $|\boldsymbol{B}| \leqslant 1$, $\boldsymbol{B} : \dot{\boldsymbol{\gamma}} = \dot{\gamma}$ and the following relation (Dean & Glowinski 2002):

$$\boldsymbol{B} = P_\Lambda\left(\boldsymbol{B} + \sigma\tau_y\dot{\boldsymbol{\gamma}}\right) \quad \forall\,\sigma > 0, \tag{A8}$$

where $P_\Lambda(\boldsymbol{q})$ is a symmetry-preserving orthogonal projection operator defined by

$$P_\Lambda(\boldsymbol{q}) = \begin{cases} \boldsymbol{q} & \text{if} \quad |\boldsymbol{q}| \leqslant 1, \\ \boldsymbol{q}/|\boldsymbol{q}| & \text{if} \quad |\boldsymbol{q}| > 1. \end{cases} \tag{A9}$$

Here $\boldsymbol{q}$ represents a non-dimensional tensor. Equation (A8) implies that $\dot{\boldsymbol{\gamma}} = \boldsymbol{0}$ when $|\boldsymbol{B} + \sigma\tau_y\dot{\boldsymbol{\gamma}}| \leqslant 1$, and $\boldsymbol{B} = \dot{\boldsymbol{\gamma}}/\dot{\gamma}$ when $|\boldsymbol{B} + \sigma\tau_y\dot{\boldsymbol{\gamma}}| > 1$, and thus (A7) is equivalent to (2.4).

The body force $\boldsymbol{f}$ on the right-hand side of (2.2) enforces a prescribed velocity boundary condition on swimmer surface S, given by

$$\boldsymbol{u} = (\boldsymbol{U} + \boldsymbol{\omega}\times\boldsymbol{r}) + \boldsymbol{u}_s \ \text{ in } \ S. \tag{A10}$$

To recover the tangential velocity (A10) on the surface of the particle, a solenoidal velocity field $\boldsymbol{u}_a$ inside the squirmer is imposed (Xia *et al.* 2025*b*,*d*). The imposed velocity leads to a zero translational and rotational velocity for the particle (i.e. $\int_P \boldsymbol{u}_a \,\mathrm{d}V = 0$ and $\int_P \boldsymbol{r} \times \boldsymbol{u}_a \,\mathrm{d}V = 0$).

For convenience, we write the dimensionless quantities in the same form as their dimensional counterparts, unless otherwise specified.

The complete set of dimensionless governing equations comprises the following three parts.

https://doi.org/10.1017/jfm.2026.12036 Published online by Cambridge University Press

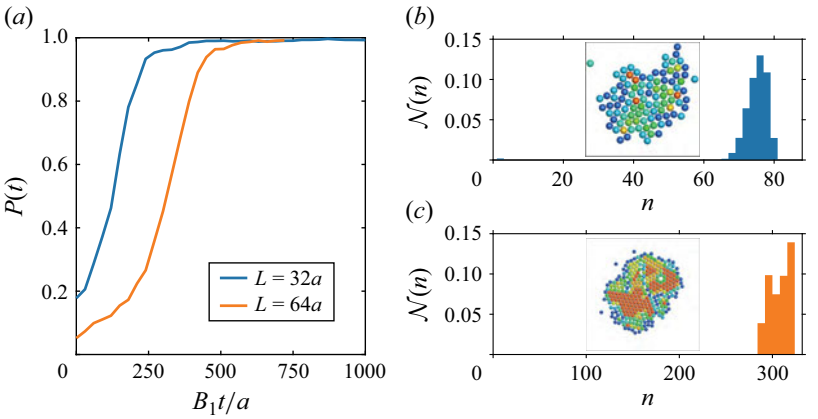


Figure 10. Effect of domain size on (*a*) temporal evolutions of the global polar order parameter $P(t)$ for neutral swimmers ($\beta = 0$, $\phi_a = 0.25$) and (*b*,*c*) normalised cluster-size distribution function $\mathcal{N}(n)$ for pullers ($\beta = 3$, $\phi_a = 0.25$) in Newtonian fluids. Insets in (*b*,*c*) show snapshots of the clusters.

(i) Equations of motion:

$$Re\left(\frac{\partial \boldsymbol{u}}{\partial t} + \boldsymbol{u}\cdot\nabla\boldsymbol{u}\right) = -\nabla p + \nabla^2\boldsymbol{u} + Bi\nabla\cdot\boldsymbol{B} + \boldsymbol{f}, \tag{A11}$$

$$\boldsymbol{u} - (\boldsymbol{U} + \boldsymbol{\omega}\times\boldsymbol{r}) - \boldsymbol{u}_a = \boldsymbol{0}. \tag{A12}$$

(ii) Continuity equation:

$$\nabla\cdot\boldsymbol{u} = \boldsymbol{0}. \tag{A13}$$

(iii) Constitutive equation:

$$\boldsymbol{B} = P_\Lambda\left(\boldsymbol{B} + \sigma Bi\dot{\boldsymbol{\gamma}}\right) \quad \forall\,\sigma > 0. \tag{A14}$$

The spatial derivatives in (A11) are evaluated using the second-order central-difference method. The convection and viscous terms are temporally integrated using the second-order Adams–Bashforth method and Crank–Nicholson method, respectively. Throughout this study, we set $\sigma = Re/(2Bi^2)$ in (A14). This choice ensures numerical stability and has been widely adopted in previous simulations of Bingham flows (Dean & Glowinski 2002). Problem (A11)–(A14) is solved in an iterative way with the fractional step time scheme (Yu & Wachs 2007). Particle quantities in (2.5)–(2.8) are updated using the first-order explicit Euler method. An efficient parallel algorithm based on message passing interface has been implemented to speed up computation.

Appendix B. Effect of the domain size

The effect of the domain width L (as well as the swimmer number N) has been examined by using a larger width $L = 64a$. Figure 10 shows the results for neutral swimmers and pullers. We can see that although the polar order evolution curves of neutral swimmers and the cluster size of pullers are affected by the domain size, the difference in the scaled results is negligible, indicating that the domain size does not influence the conclusions from our work. Similar trends were observed in viscoplastic fluids, and are therefore not shown here for brevity.

https://doi.org/10.1017/jfm.2026.12036 Published online by Cambridge University Press

References

Aceves-Sanchez, P., Degond, P., Keaveny, E.E., Manhart, A., Merino-Aceituno, S. & Peurichard, D. 2020 Large-scale dynamics of self-propelled particles moving through obstacles: model derivation and pattern formation. *Bull. Math. Biol.* **82**, 129.

Aditi Simha, R. & Ramaswamy, S. 2002 Hydrodynamic fluctuations and instabilities in ordered suspensions of self-propelled particles. *Phys. Rev. Lett.* **89**, 058101.

Aranson, I.S. 2022 Bacterial active matter. *Rep. Prog. Phys.* **85** (7), 076601.

Balmforth, N.J. & Hewitt, D.R. 2025 The implications of a fluid yield stress. *J. Fluid Mech.* **1011**, P1.

Baskaran, A. & Marchetti, M.C. 2008 Enhanced diffusion and ordering of self-propelled rods. *Phys. Rev. Lett.* **101** (26), 268101.

Bechinger, C., Di Leonardo, R., Löwen, H., Reichhardt, C., Volpe, G. & G., Volpe 2016 Active particles in complex and crowded environments. *Rev. Mod. Phys.* **88**, 045006.

Be'er, A., Ilkanaiv, B., Gross, R., Kearns, D.B., Heidenreich, S., Bär, M. & Ariel, G. 2020 A phase diagram for bacterial swarming. *Commun. Phys.* **3** (1), 66.

Blake, J.R. 1971 A spherical envelope approach to ciliary propulsion. *J. Fluid Mech.* **46** (1), 199–208.

Brady, J.F. & Bossis, G. 1988 Stokesian dynamics. *Annu. Rev. Fluid Mech.* **20**, 111–157.

Bricard, A., Caussin, J.-B., Desreumaux, N., Dauchot, O. & Bartolo, D. 2013 Emergence of macroscopic directed motion in populations of motile colloids. *Nature* **503**, 95–98.

Cates, M.E. & Tailleur, J. 2015 Motility-induced phase separation. *Annu. Rev. Condens. Matter Phys.* **6** (1), 219–244.

Chamolly, A. & Ishikawa, T. 2026 Self-organised structures in mixed active–passive suspensions due to hydrodynamic interactions. *J. Fluid Mech.* **1030**, A22.

Dean, E.J. & Glowinski, R. 2002 Operator-splitting methods for the simulation of Bingham visco-plastic flow. *Chin. Ann. Maths* **23** (02), 187–204.

Dombrowski, C., Cisneros, L., Chatkaew, S., Goldstein, R.E. & Kessler, J.O. 2004 Self-concentration and large-scale coherence in bacterial dynamics. *Phys. Rev. Lett.* **93** (9), 098103.

Drescher, K., Dunkel, Jörn, Cisneros, L.H., Ganguly, S. & Goldstein, R.E. 2011 Fluid dynamics and noise in bacterial cell-cell and cell-surface scattering. *Proc. Natl Acad. Sci.* **108** (27), 10940–10945.

Eastham, P.S., Mohammadigoushki, H. & Shoele, K. 2022 Squirmer locomotion in a yield stress fluid. *J. Fluid Mech.* **948**, A54.

Elgeti, J., Winkler, R.G. & Gompper, G. 2015 Physics of microswimmers—single particle motion and collective behavior: a review. *Rep. Prog. Phys.* **78** (5), 056601.

Fily, Y. & Marchetti, M.C. 2012 Athermal phase separation of self-propelled particles with no alignment. *Phys. Rev. Lett.* **108**, 235702.

Gompper, G., *et al.* 2025 The 2025 motile active matter roadmap. *J. Phys.: Condens. Matter* **37**, 143501.

Hewitt, D.R. & Balmforth, N.J. 2017 Taylor's swimming sheet in a yield-stress fluid. *J. Fluid Mech.* **828**, 33–56.

Hewitt, D.R. & Balmforth, N.J. 2022 Locomotion with a wavy cylindrical filament in a yield-stress fluid. *J. Fluid Mech.* **936**, A17.

Ishikawa, T. 2008 Coherent structures in monolayers of swimming particles. *Phys. Rev. Lett.* **100** (8), 088103.

Ishikawa, T. 2019 Swimming of ciliates under geometric constraints. *J. Appl. Phys.* **125**, 200901.

Ishikawa, T. 2024 Fluid dynamics of squirmers and ciliated microorganisms. *Annu. Rev. Fluid Mech.* **56** (1), 119–145.

Ishikawa, T. 2025 Transport phenomena in microswimmer suspensions: migration, collective motion, diffusion and rheology. *J. Fluid Mech.* **1016**, P1.

Ishikawa, T., Locsei, J.T. & Pedley, T.J. 2008 Development of coherent structures in concentrated suspensions of swimming model micro-organisms. *J. Fluid Mech.* **615**, 401–431.

Ishikawa, T., Simmonds, M.P. & Pedley, T.J. 2006 Hydrodynamic interaction of two swimming model micro-organisms. *J. Fluid Mech.* **568**, 119–160.

Kantsler, V., Dunkel, J., Polin, M. & Goldstein, R.E. 2013 Ciliary contact interactions dominate surface scattering of swimming eukaryotes. *Proc. Natl Acad. Sci.* **110** (4), 1187–1192.

Keller, S.R. & Wu, T.Y. 1977 A porous prolate-spheroidal model for ciliated micro-organisms. *J. Fluid Mech.* **80** (2), 259–278.

Kim, S. & Karrila, S.J. 2005 *Microhydrodynamics - Principles and Selected Applications*. Dover Publications.

Kobayashi, T., Molina, J.J. & Yamamoto, R. 2024 Propulsion of a chiral swimmer in viscoelastic fluids. *Phys. Rev. Res.* **6**, 033304.

Kyoya, K., Matsunaga, D., Imai, Y., Omori, T. & Ishikawa, T. 2015 Shape matters: near-field fluid mechanics dominate the collective motions of ellipsoidal squirmers. *Phys. Rev. E* **92** (6), 063027.

https://doi.org/10.1017/jfm.2026.12036 Published online by Cambridge University Press

LAUGA, E. 2020 *The Fluid Dynamics of Cell Motility*. Cambridge University Press.
LAUGA, E. & POWERS, T.R. 2009 The hydrodynamics of swimming microorganisms. *Rep. Prog. Phys.* **72** (9), 096601.
LEVIS, D. & BERTHIER, L.2014 Clustering and heterogeneous dynamics in a kinetic Monte Carlo model of self-propelled hard disks. *Phys. Rev. E* **89** (6), 062301.
LI, G. & ARDEKANI, A.M. 2016 Collective motion of microorganisms in a viscoelastic fluid. *Phys. Rev. Lett.* **117** (11), 118001.
LIAO, W. & ARANSON, I.S. 2023 Viscoelasticity enhances collective motion of bacteria. *PNAS Nexus* **2** (9), pgad291.
LIGHTHILL, M.J. 1952 On the squirming motion of nearly spherical deformable bodies through liquids at very small Reynolds numbers. *Commun. Pure Appl. Maths* **5** (2), 109–118.
LIN, Z. & GAO, T. 2019 Direct-forcing fictitious domain method for simulating non-Brownian active particles. *Phys. Rev. E* **100** (1), 013304.
LIU, S., SHANKAR, S., MARCHETTI, M.C. & WU, Y. 2021 Viscoelastic control of spatiotemporal order in bacterial active matter. *Nature* **590** (7844), 80–84.
NAZARI, F., SHOELE, K. & MOHAMMADIGOUSHKI, H. 2023 Helical locomotion in yield stress fluids. *Phys. Rev. Lett.* **130** (11), 114002.
QI, K., WESTPHAL, E., GOMPPER, G. & WINKLER, R.G. 2022 Emergence of active turbulence in microswimmer suspensions due to active hydrodynamic stress and volume exclusion. *Commun. Phys.* **5** (1), 49.
RAMASWAMY, S. 2010 The mechanics and statistics of active matter. *Annu. Rev. Condens. Matter Phys.* **1** (1), 323–345.
REDNER, G.S., HAGAN, M.F. & BASKARAN, A. 2013 Structure and dynamics of a phase-separating active colloidal fluid. *Phys. Rev. Lett.* **110**, 055701.
SAINTILLAN, D. & SHELLEY, M.J. 2007 Orientational order and instabilities in suspensions of self-locomoting rods. *Phys. Rev. Lett.* **99** (5), 058102.
SAINTILLAN, D. & SHELLEY, M.J. 2008 Instabilities and pattern formation in active particle suspensions: kinetic theory and continuum simulations. *Phys. Rev. Lett.* **100** (17), 178103.
SPAGNOLIE, S.E. & UNDERHILL, P.T. 2023 Swimming in complex fluids. *Annu. Rev. Condens. Matter Phys.* **14** (2023), 381–415.
THEERS, M., WESTPHAL, E., GOMPPER, G. & WINKLER, R.G. 2016 Modeling a spheroidal microswimmer and cooperative swimming in a narrow slit. *Soft Matt.* **12** (35), 7372–7385.
THEERS, M., WESTPHAL, E., QI, K., WINKLER, R.G. & GOMPPER, G. 2018 Clustering of microswimmers: interplay of shape and hydrodynamics. *Soft Matt.* **14**, 8590–8603.
TUNG, C.-K., LIN, C., HARVEY, B., FIORE, A.G., ARDON, F., WU, M. & SUAREZ, S.S. 2017 Fluid viscoelasticity promotes collective swimming of sperm. *Sci. Rep.* **7** (1), 3152.
WENSINK, H.H., *et al.* 2012 Meso-scale turbulence in living fluids. *Proc. Natl Acad. Sci.* **109** (36), 14308–14313.
WU, Z., CHEN, Y., MUKASA, D., GAO, W. & PAK, O.S. 2020 Medical micro/nanorobots in complex media. *Chem. Soc. Rev.* **49**, 8088–8112.
WU-ZHANG, B., FEDOSOV, D.A. & GOMPPER, G. 2024 Collective behavior of squirmers in thin films. *Soft Matt.* **20**, 5687–5702.
XIA, Y., YU, Z., HU, X., ZHU, C. & LIN, Z. 2025*a* Pairwise interactions of active particles in a yield stress fluid. *J. Non-Newtonian Fluid Mech.* **345**, 105486.
XIA, Y., YU, Z., LIN, J., LIN, Z. & HU, X. 2025*b* Dynamics of a spheroidal squirmer interacting with a cylindrical obstacle. *Soft Matt.* **21** (17), 3267–3277.
XIA, Y., YU, Z., LIN, Z. & ISHIKAWA, T. 2025*c* Swimming and mixing of an ellipsoidal squirmer in a viscoplastic fluid. *J. Fluid Mech.* **1015**, A12.
XIA, Y., YU, Z., ZHANG, M., LIN, Z. & OUYANG, Z. 2025*d* Swimming dynamics of a spheroidal microswimmer near a wall. *Phys. Rev. E* **111** (4), 045106.
YOSHINAGA, N. & LIVERPOOL, T.B. 2018 From hydrodynamic lubrication to many-body interactions in dense suspensions of active swimmers. *Eur. Phys. J. E* **41**, 76.
YU, Z. & SHAO, X. 2007 A direct-forcing fictitious domain method for particulate flows. *J. Comput. Phys.* **227** (1), 292–314.
YU, Z. & WACHS, A. 2007 A fictitious domain method for dynamic simulation of particle sedimentation in Bingham fluids. *J. Non-Newtonian Fluid Mech.* **145** (2-3), 78–91.
ZHANG, M., YU, Z., OUYANG, Z., XIA, Y. & LIN, Z. 2024 Numerical study of collective motion of microswimmers in Giesekus viscoelastic fluids. *J. Non-Newtonian Fluid Mech.* **329**, 105245.

https://doi.org/10.1017/jfm.2026.12036 Published online by Cambridge University Press

ZHANG, M., YU, Z., XIA, Y., ZHU, C., LIN, Z. & LU, W. 2025 The collective motion of a binary pusher-puller mixture in viscoelastic fluids. *Engng Applics Commun. Fluid Mech.* **19** (1), 2547249.

ZHOU, T. & BRADY, J.F. 2026 Hydrodynamic interactions destroy motility-induced phase separation in active suspensions. *Phys. Rev. Lett.* **136** (8), 088301.

ZÖTTL, A. & STARK, H. 2014 Hydrodynamics determines collective motion and phase behavior of active colloids in quasi-two-dimensional confinement. *Phys. Rev. Lett.* **112** (11), 118101.

ZÖTTL, A. & STARK, H. 2023 Modeling active colloids: from active Brownian particles to hydrodynamic and chemical fields. *Annu. Rev. Condens. Matter Phys.* **14**, 109–127.

https://doi.org/10.1017/jfm.2026.12036 Published online by Cambridge University Press